

# Aerodynamic Topology Optimization: Some Observations on Hysteresis in Separated Flows

Carsten Othmer\*

*Electronics Research Laboratory, Volkswagen Group of America Inc., Belmont, CA 94002, USA*

David E. Manosalvas-Kjono†

*Stanford University, Stanford, CA 94305, USA*

Antony Jameson‡

*Stanford University, Stanford, CA 94305, USA*

Juan J. Alonso§

*Stanford University, Stanford, CA 94305, USA*

Fluid dynamic topology optimization is a well-established concept for ducted flows, which is widely applied in the automotive industry. The application of this kind of optimization in external aerodynamics has however, received only little attention so far. The current study is intended as the starting point of exploring the potential of topology optimization in external aerodynamics, specifically for separated turbulent flows. For our investigations, we therefore choose a standard benchmark case for this kind of flows: the 2D Ahmed body with a slant angle of  $25^\circ$ , at a Reynolds number corresponding to car aerodynamics of  $4 \cdot 10^6$ . We introduce the concept and the numerical realization of fluid dynamic topology optimization, apply it to the Ahmed body test case and explore in detail the hysteresis behavior observed upon optimizing the rear end of the body. We conclude that topology optimization is a powerful tool also for external aerodynamics, whose working principle allows to discover and exploit hysteresis phenomena, that, in the present case, lead to an enormous cost function improvement with minimal geometric changes.

## I. Introduction

Adjoint-based optimization<sup>1–5</sup> has long been recognized to be efficient for design tasks with large numbers of design variables. Its underlying principle, the adjoint method, allows for a very elegant computation of sensitivities, i. e. of the derivative of the objective function with respect to (w. r. t.) the design variables. The computational effort is thereby independent of the number of design variables and just involves one solve of the adjoint counterparts of the governing equation system. When applied to a surface mesh representation or a volume mesh of the part to be optimized, information like the one depicted in Fig. 1, for which the term “sensitivity maps” was coined, can be generated: A surface sensitivity map indicates for each surface node how the objective function changes w. r. t. an infinitesimally small normal displacement of this surface node. On the other hand, a volume sensitivity map represents for each volume cell the sensitivity of the objective function w. r. t. a change of permeability of this volume cell. Both sensitivity maps give precise indications on where and how to change the geometry – perturb the surface inwards or outwards, and remove counterproductive cells from the flow domain, respectively – in order to improve the objective function. In this way, surface sensitivity maps give naturally rise to *shape optimization* procedures, while volume sensitivity maps are key to fluid dynamic *topology optimization*.

Topology optimization is a well-established tool in computational structure mechanics<sup>6</sup> with widespread industrial use. In its simplest realization, a topological optimization starts from the available design domain filled up entirely with solid material of a certain density. In an iterative fashion, the given loads are applied,

---

\*Senior Researcher and Project Lead; Visiting Scholar at Stanford University, Department of Aeronautics & Astronautics.

†PhD candidate, Department of Aeronautics & Astronautics, AIAA Student Member.

‡Research Professor, Department of Aeronautics & Astronautics, AIAA Fellow.

§Professor, Department of Aeronautics & Astronautics, AIAA Associate Fellow.

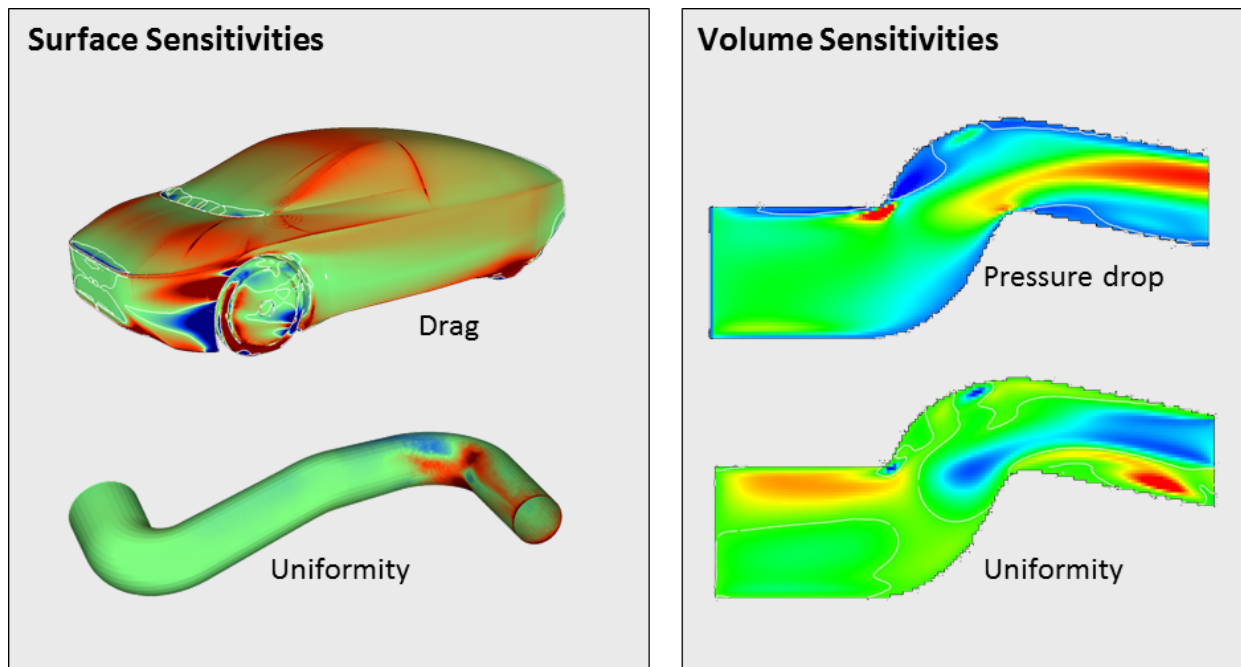


Figure 1. Sensitivity maps: Surface sensitivity maps (left) display the gradient of the cost function w. r. t. normal displacements of the surface. In red areas, a movement away from the fluid (i. e. inwards for the car, outwards for the pipe) would result in an improvement of the cost function. Contrarily, blue areas indicate the regions where a surface perturbation towards the fluid improves performance, while modifications in greenish surface sections have little effect on the cost function. The white lines on the car body are the isolines of zero sensitivity, i. e. the borderline between favorable inward and outward movement. Topological or volume sensitivities (shown on the right hand-side for a cut through an airduct) represent the cost function gradient w. r. t. changes of the individual cell permeability. Blue volume sections are those where decreasing the cell permeability (by adding a porosity-based friction term) would improve the cost function. Those areas are thus counterproductive to the component's fluid dynamic performance and should be removed - the basis of CFD topology optimization.

the stresses are computed all over the domain and the areas with low stresses are weakened by assigning a lower density to them. After several iterations, this method retains high-density material only in regions that are critical to fulfill the structural task, and in this way generates optimal lightweight structural designs. It delivers an unbiased design from scratch that automatically fulfills the installation space constraints.

It almost comes as a surprise that it took until 2003 until this elegant concept was transferred to fluid dynamics: Independently of each other, Borrvall and Petersson<sup>7</sup> and Klimetzek<sup>8</sup> presented the first topological optimization methods for ducted flows. Analogously to its structural mechanic archetype, their fluid dynamic topology optimization starts from a completely flooded computational domain, uses some local criterion to identify those areas that are counterproductive w. r. t. the chosen objective function, and iteratively “punishes” or removes them from the fluid domain. As a result, the remaining areas constitute the optimal duct between inlet(s) and outlet(s) of the given installation space.

Despite being based on the same concept of flow optimization, these two approaches exhibit significant differences. Klimetzek's method is a rather pragmatic solution: The local criterion that is employed to identify counterproductive cells is the deviation between the actual velocity direction and a desired direction computed as polygonal traces between inlet and outlet. If this deviation exceeds a certain angle, the corresponding cells are blocked for the fluid. This criterion allows to efficiently remove unwanted recirculation areas from the flow and – albeit being used for other cost function as well – is therefore ideally suited to reduce the pressure drop. From the date of its original publication, Klimetzek's method has already been applicable to three-dimensional turbulent Navier-Stokes flows and is seeing a continuously increasing number of successful applications in industrial flow optimization under the brand Tosca Fluid<sup>®</sup>.<sup>9</sup>

In contrast, the method proposed by Borrvall and Petersson was restricted to two-dimensional Stokes flows between parallel plates, and the punishment of counterproductive areas is performed by locally decreasing the distance between the plates – until zero upon convergence. What inspired a series of subsequent research

works is, however, the versatility of their approach that lies in the way how they identify counterproductive fluid cells: by computing actual sensitivities via the adjoint method.

In order to extend the Borrvall-Petersson method towards three-dimensional flows, the punishment via plate distance was replaced by introducing a Darcy porosity term  $-\alpha \mathbf{v}$  into the momentum equation (see Gersborg-Hansen et al.<sup>10</sup> and Othmer and Grahs<sup>11</sup> for a finite-element and a finite-volume implementation, respectively). The individual cell porosities allow a continuous transition between fluid ( $\alpha = 0$ ) and solid ( $\alpha = \alpha_{max}$ ) and act as the actual design variables of the optimization problem. With this setting, topological sensitivity maps like those shown in Fig. 1 are nothing but the derivative of the cost function w.r.t. an increase in the local Darcy coefficient  $\alpha$ .

After the principal feasibility of laminar Navier-Stokes topology optimization was first demonstrated via Automatic Differentiation of an academic CFD code,<sup>12</sup> the concept was implemented for turbulent flows via a continuous adjoint<sup>13</sup> – albeit under the assumption of “frozen turbulence”, i.e. fully neglecting the variation of the turbulent flow quantities. Finally, the development of a continuous adjoint turbulence model<sup>14,15</sup> now allows to run topology optimization for turbulent Navier-Stokes flows under full consideration of variations in the turbulent fields.<sup>16</sup>

As topology optimization is not only very fast but also mimics the classical way of part design that is driven by installation space constraints, the integration of this method in the regular automotive design process was quite straightforward. A number of ducted flow applications are today routinely optimized via adjoint-based topology optimization,<sup>17</sup> and the uptake and further development of the basic adjoint code by other researchers lead to remarkable advances,<sup>18–21</sup> especially in the area of topology optimization for exhaust systems.<sup>22,23</sup>

The transfer of topology optimization to external aerodynamics has, however, received almost no attention so far. To our knowledge, the only published effort in that direction was undertaken by Kondoh et al.,<sup>24</sup> who optimized 2D airfoils in laminar flow regimes. The present investigation is intended to extend that study towards turbulent, incompressible, separated flow. To that end, we apply topology optimization to a 2D version of the 25° slant Ahmed body<sup>25</sup> along the following lines: Section II introduces the test case, the flow field and the sensitivities. The actual topology optimization procedure and its results for the chosen test case are described in section III, while section IV is dedicated to scrutinizing the observed hysteresis behavior and its dependence on the slant angle. Section V finally draws conclusions on the suitability and possible added-value of topology optimization for external aerodynamics.

## II. The Test Case: Flow Field and Sensitivities

For the 25° slant angle version of the Ahmed body, a low-Reynolds mesh of 107,000 trias and quads was created, including 48 quad layers with a wall distance of the first node of  $10^{-3} mm$  and a growth rate of 1.2 (see Figure 2). In a windtunnel box extending 20 body lengths in horizontal and 10 in vertical direction, the steady-state incompressible, turbulent air flow around the Ahmed body was computed using OpenFOAM<sup>®</sup>,<sup>26</sup> thereby employing the Reynolds-Averaged Navier-Stokes (RANS) solver “simpleFoam” and the Spalart-Allmaras turbulence model. The inlet velocity was chosen to be  $60 m/s$ , resulting in a Reynolds number of  $Re = 4 \cdot 10^6$ . A homogeneous Dirichlet boundary condition for the static pressure at the outlet and slip-conditions for both road and windtunnel roof complete the setup.

For the solution of the adjoint equations and the topology optimization, we employ the incompressible adjoint RANS solver HELYXAdjoint<sup>®</sup>.<sup>27</sup> It is an industrialized and much enhanced version of the original “frozen turbulence” continuous adjoint formulation of Othmer.<sup>13</sup> Starting from the primal equations for velocity  $\mathbf{v}$  and pressure  $p$ ,

$$(\mathbf{v} \cdot \nabla) \mathbf{v} = -\nabla p + \nabla \cdot (2\nu \mathbf{D}(\mathbf{v})) - \alpha \mathbf{v} \quad (1)$$

$$\nabla \cdot \mathbf{v} = 0, \quad (2)$$

where  $\nu$  stands for the effective kinematic viscosity,  $\mathbf{D}(\mathbf{v}) = \frac{1}{2} (\nabla \mathbf{v} + (\nabla \mathbf{v})^T)$  for the rate of strain tensor, and  $\alpha$  for the porosity distribution developing through the topology optimization process, it solves the following set of adjoint equations:

$$-(\mathbf{v} \cdot \nabla) \mathbf{u} - \nabla \mathbf{u} \cdot \mathbf{v} = -\nabla q + \nabla \cdot (2\nu \mathbf{D}(\mathbf{u})) - \alpha \mathbf{u} - \frac{\partial J_\Omega}{\partial \mathbf{v}} \quad (3)$$

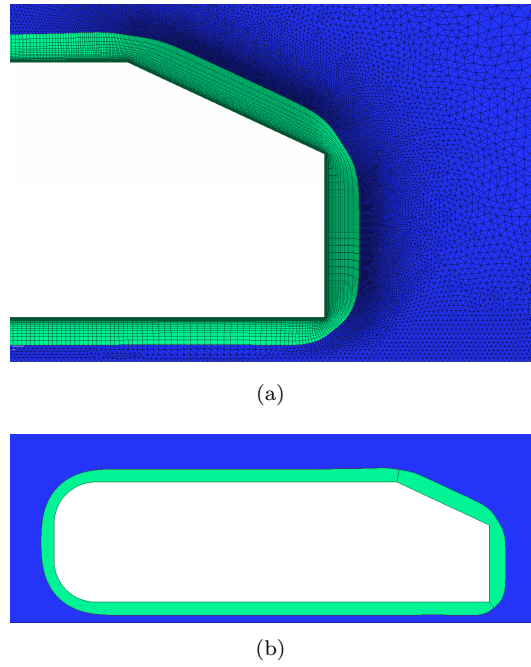


**Figure 2.** Ahmed body mesh: (a) Details of the mesh around the back of the body. The 48 quad-layers are shown in green, the tria-mesh area in blue. (b) The design domain (green) corresponds to the extent of the quad layers.

$$\nabla \cdot \mathbf{u} = \frac{\partial J_{\Omega}}{\partial p}, \quad (4)$$

with  $\mathbf{u}$  and  $q$  denoting adjoint velocity and adjoint pressure, respectively.  $J_{\Omega}$  is the volume contribution of the spatially decomposed cost function  $J$ ,

$$J = \int_{\Gamma} J_{\Gamma} d\Gamma + \int_{\Omega} J_{\Omega} d\Omega, \quad (5)$$

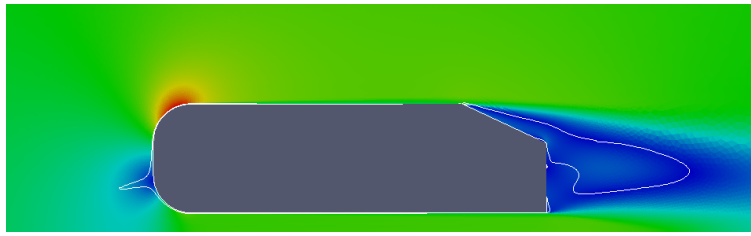
with  $\Omega$  being the interior of the design domain and  $\Gamma = \partial\Omega$  its boundary. Along with suitable boundary conditions<sup>13</sup> for the adjoint variables  $\mathbf{u}$  and  $q$ , the adjoint flow field can be computed and allows to determine the desired (volume-normalized) topological and (surface-normalized) shape sensitivities as

$$\frac{\partial J}{\partial \alpha} = \mathbf{u} \cdot \mathbf{v} \quad \text{and} \quad \frac{\partial J}{\partial \beta} = -\nu \partial_n \mathbf{u} \cdot \partial_n \mathbf{v}, \quad (6)$$

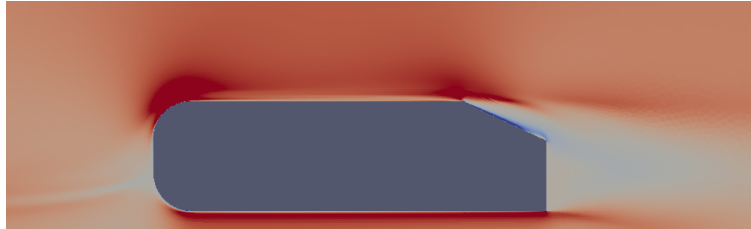
where  $\beta$  denotes the normal node displacement.

The cost function of interest in our case is the drag force exerted by the flow on the Ahmed body. However, our current formulation of the primal and the adjoint does not account for the drag contribution of the porous medium (and of the porous/fluid interface) that builds up during the optimization. We therefore chose the dissipated power in the whole domain as the relevant cost function entering the adjoint equation system. As slip conditions are used on the road and the windtunnel roof, the actual drag experienced by the Ahmed body and the porosity additions should be equal to the dissipated power divided by the constant inlet velocity. The sensitivities computed in this way are therefore directly proportional to the actually desired drag sensitivities. They are displayed in Figs. 3 and 4.

As expected, the topological sensitivities (Fig. 3) indicate that a large portion of the separation bubble is counterproductive in terms of drag and should be “filled” with solid material. Interestingly, they also allude to a guiding vane at the front face of the Ahmed body right at the stagnation point in order to divide the flow and guide it smoothly around the otherwise bluff body. In contrast, the shape sensitivities (Fig. 4) exhibit the typical behavior for separated flows: huge values of opposite sign at the two cells adjacent to the sharp edges where the separation takes place. If there is in fact an added-value of using topological sensitivities/optimization vs. shape sensitivities/optimization is one of the objectives of this study.

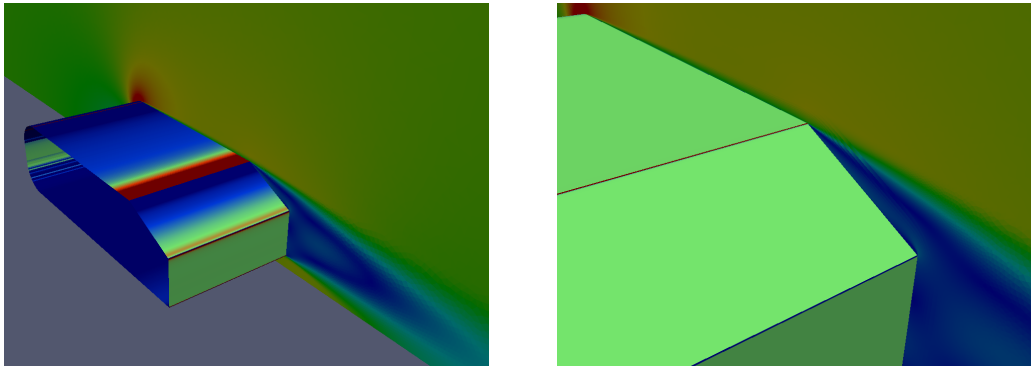


(a)

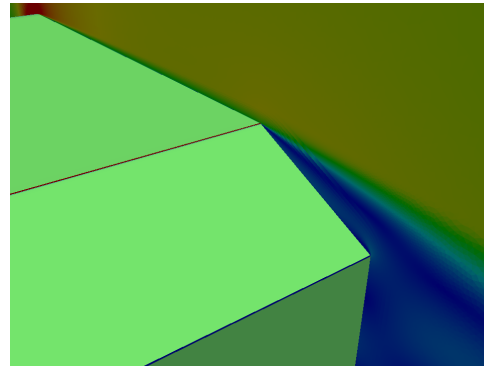


(b)

Figure 3. Baseline geometry: (a) Velocity field and isolines of zero sensitivity (white). Note the massive separation at the top edge of the slanted surface. (b) Topological sensitivities for dissipated power. The favorable areas are red, while counterproductive areas have blueish color.



(a)



(b)

Figure 4. Surface sensitivities: (a) The cutting plane shows the velocity field, and the shape sensitivities are depicted on the body (extruded for visualization purposes). Red indicates a favorable outward surface displacement, blue an inward displacement. (b) The same quantities as in (a), but the sensitivities are scaled by  $10^4$ . Note the sensitivity spikes at the edges.

### III. Topology Optimization Results

Starting point for the topology optimization are the fully converged primal and adjoint solutions of the base line case as presented in the previous section. The optimization is then carried out with HELYXAdjoint<sup>®</sup> in one-shot mode: Based on the topological sensitivities computed from the concurrently running primal and adjoint solver, the Darcy porosity field  $\alpha$  is updated via a steepest descent algorithm with fixed step size. To make the case more realistic in view of actual vehicle optimization, we restrict the porosity update to the immediate vicinity of the original Ahmed body defined by the extent of the quad-mesh surface layers (see Fig. 2). Moreover, in order to avoid the buildup of porous islands, the porosity update takes place in “propagating front” mode:<sup>28</sup> New porosity can only grow from solid surfaces or other porous cells. The porosity is arbitrarily capped at  $\alpha_{max} = 10^6$ , at which value porous cells are practically impermeable and can be regarded as solid.

Fig. 5 shows the resulting porosity distribution and contrasts the optimized flow field with the one of the original Ahmed body. Apart from minor additions at the front, the optimal topology results in a smaller slant angle ( $23.2^\circ$ ) and an appendix/spoiler. The shape of the latter is, however, mainly determined by the definition of the design area (see Fig. 2). While the flow originally detaches at the top edge of the slanted surface, thereby generating a huge recirculation area, these moderate porosity additions manage to guide the flow around the top edge and delay the separation until the trailing edge (Fig. 6), thereby reducing drag by almost 50%.

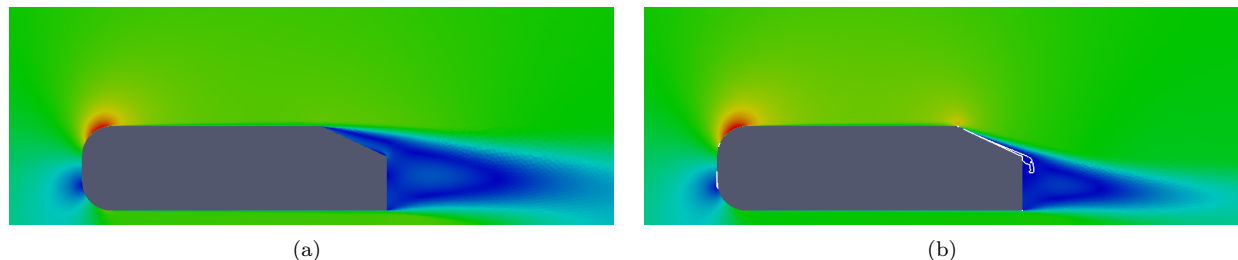


Figure 5. Topology optimization result: (a) Original velocity field with separation at the top edge. (b) Optimized velocity field and isocontours of resulting porosity (isovalued  $\alpha = 10^5$ ). Through the addition of a thin porosity wedge, which effectively reduces the slant angle, and a spoiler-like appendix, the flow stays attached until the trailing edge. The dissipated power is reduced to 52% of the original value.

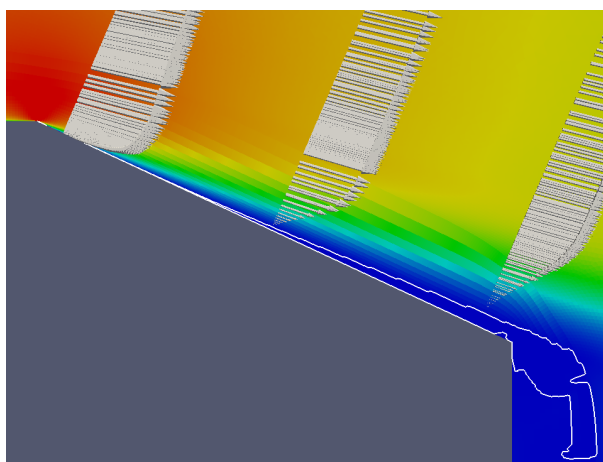


Figure 6. Boundary layer along the slanted surface of the optimized case: Shown are the velocity vectors and the velocity magnitude (color-coded). Within the porous area, the velocity is practically zero, indicating that the chosen value for  $\alpha_{\max}$  is large enough to represent fully blocked cells. The shear stress on the built-up porosity decreases but stays non-zero all along the slanted surface.

When investigating the course of the optimization (see Fig. 7), the following can be observed: After the initial transients have gone, the buildup of porosity starts at the leading edge of the slanted surface and continues downward, thereby “bending” the flow around the corner and attaching it to the newly developed surface. Once the flow is attached further down, porosity is continuously removed upstream to some degree (the porosity wedge is getting thinner), i. e. part of the porosity is only temporarily required to guide the flow along the slant. This alludes already to the hysteresis effect to be investigated in more detail in the next section.

First, however, the resulting porosity distribution needs to be recast into a new geometry for a valid assessment of the obtained improvement, specifically to allow for a proper wall treatment at the newly formed solid surfaces. In order to focus on the effects at the rear end of the body, we thereby omitted the porosity changes at the front. When running a RANS simulation on this new geometry from scratch (Fig. 8a), the flow separates at the beginning of the slanted surface – in contrast to the result of the topology optimization (Fig. 5b). Apparently, the guiding effect of the transitionally built up porosity is instrumental for the flow to stay attached.

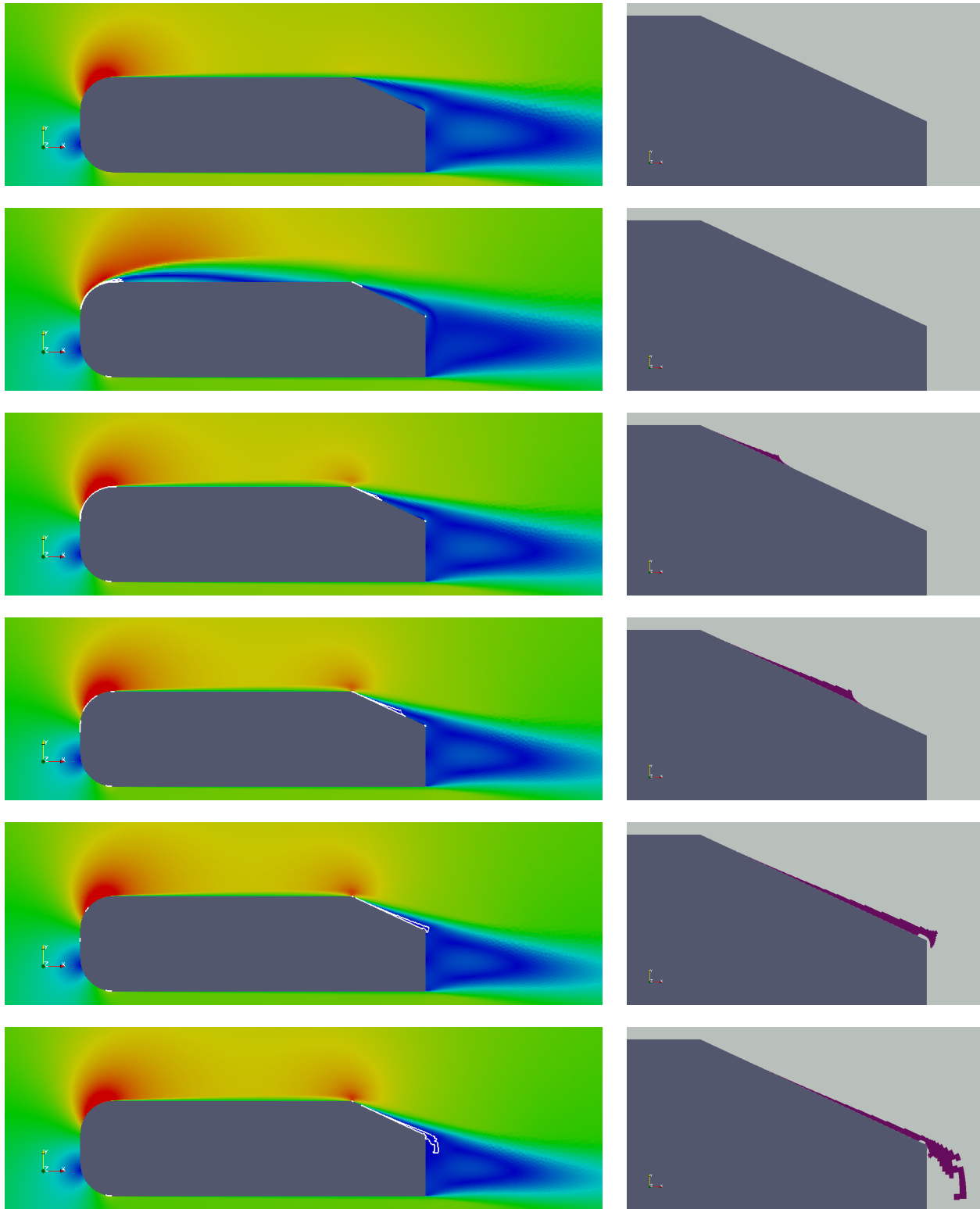


Figure 7. Snapshots of the evolution of velocity field (left column) and porosity (right column) at 0, 20, 40, 60, 80 and 100% of the total optimization span: After some transients in the early phase of the optimization with prominent porosity areas emerging at the front (2nd row), the rear porosity builds up steadily, starting from the top edge and running down along the slanted surface, thereby “dragging” the flow with it. Note how the porosity wedge is continuously being thinned out in the course of the optimization as soon as the flow attaches further down.

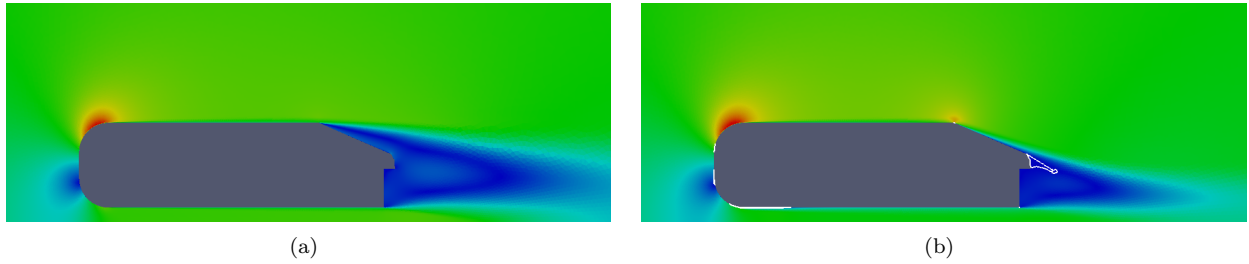


Figure 8. Flow field around the rebuilt geometry of Fig. 5b: (a) When starting the computation from scratch, the flow separates again at the top edge (dissipated power 97%). (b) When running a topology optimization on the rebuilt geometry, the transient buildup of porosity along the slanted surface leads to an attachment of the flow and, in combination with an extended spoiler, reduces the dissipated power to 43%.

This hypothesis is verified by running a topology optimization on the *rebuilt* geometry. As can be seen in Fig. 8b, it leads indeed to an attached flow. After a short transient phase, the porosity in the rear shows the same behavior as for the optimization of the original: The buildup starts at the top edge, moves downwards along with the attached flow while thinning out upstream. In this case, as the slant angle is already optimal, the porosity vanishes even entirely along the slant. As compared to the original optimization result, the dissipated power is further reduced (43% vs. 52%). This is due to the fact that, here, porosity buildup was allowed also outside the green area of Fig. 2, and a real spoiler can form (Fig. 8b).

However, our only interest in this optimization result is in using its velocity and pressure distribution as a seed solution for the rebuilt geometry of the first optimization. Initializing the flow around the rebuilt geometry with the attached flow obtained via topology optimization of this same geometry results in a stably attached flow (see Fig. 9). The dramatic cost function improvement of the original topology optimization is confirmed. It is in fact even superseded by a few percent, presumably due to the additional dissipated power of the ragged porosity surface, which is smoothed out upon rebuilding the geometry.

As a result, the current geometry obviously supports two dramatically different solutions, depending on the history of the flow – a classical hysteresis behavior that we are going to scrutinize in the following section.

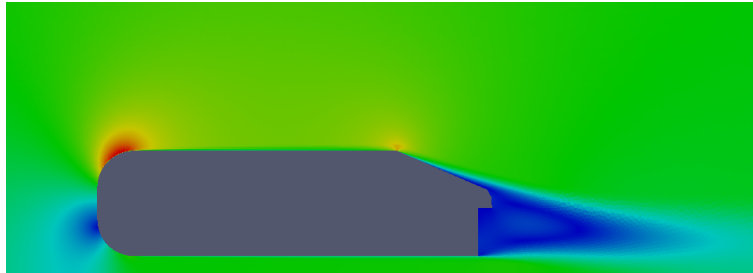


Figure 9. The velocity field for the rebuilt geometry of Fig. 5b, initialized with the attached flow field of Fig. 8b. The flow remains attached and dissipated power is reduced to 49%.

#### IV. Scrutinizing the Hysteresis Behavior

The transition between the two hysteresis states was so far performed by building up porosity during a topology optimization. This is not a practical solution – neither for the possible real-life technical exploitation of this phenomenon nor for further numerical investigation. From now on, we therefore use a small temporary suction jet as a trigger. After some trial and error, a configuration with a suction jet of 1 mm width (corresponding to 1/250th of the slant length) a few mm downstream of the top edge, operating with a normal velocity of 30 m/s (i. e. at 50% of the windtunnel inflow velocity) was figured out to be useful for our purposes (and also technically feasible in a possible real car application). In addition, we switch from steady-state RANS to unsteady RANS (URANS, with “*pisoFoam*”<sup>26</sup> and a time step of  $10^{-5}$  s) to capture possible unsteady effects and better assess the stability of the obtained solutions.

For the sake of coherence with the findings of the previous section, we first confirm the hysteresis behavior by applying the new numerical setup to three geometries: (1) the original, (2) the rebuilt version of the optimization result (i. e. with changed slant angle and spoiler), and (3) the optimized version, but rebuilt without the spoiler. The third case will allow us to separate the effects stemming from slant angle change and spoiler, respectively, and to explore the broader picture of hysteresis w. r. t. slant angle as the single parameter.

For these three geometries, the following procedure is applied: Running URANS from scratch with the jet switched off until a first steady state is reached, switching on the jet until a second steady state is reached (100 *ms* turned out to be enough) and finally switching off the jet again to let the flow evolve towards a third steady state. The results are displayed in Fig. 10. For all three geometries, the flow is separated in the first steady state, and fully attached in the second steady state (i. e. when the jet is operational). The behavior upon switching the jet off differs significantly, though: While for the original geometry, the flow separates again, resulting in a drag coefficient of  $C_D = 0.4299$ , it stays stably attached for both rebuilt geometries (with drag coefficients of 0.1999 with spoiler and 0.2144 without, respectively). These findings confirm the hysteresis observations of the previous section and indicate that it is actually the changed slant angle and not the spoiler that is responsible for this behavior. We note, however, the beneficial effect of the spoiler on the drag coefficient, which underpins the usefulness of topology optimization as opposed to pure shape optimization.

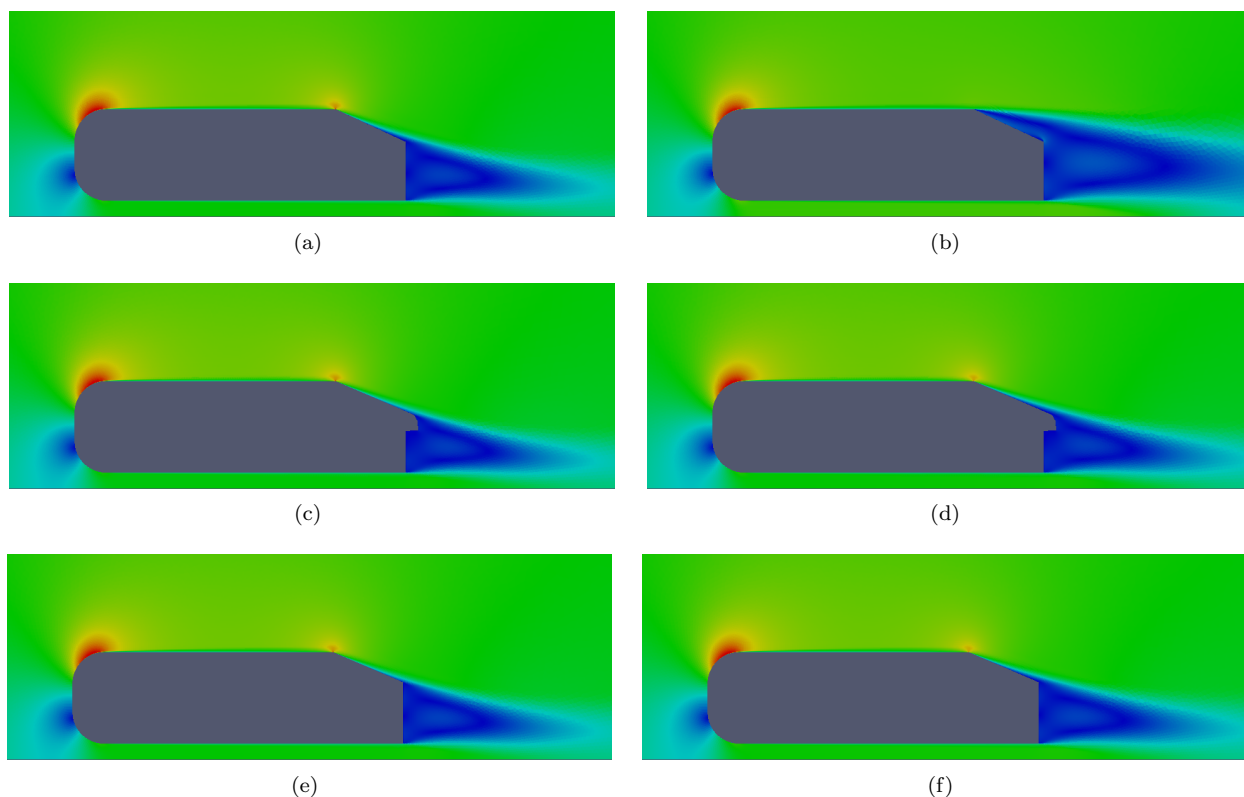
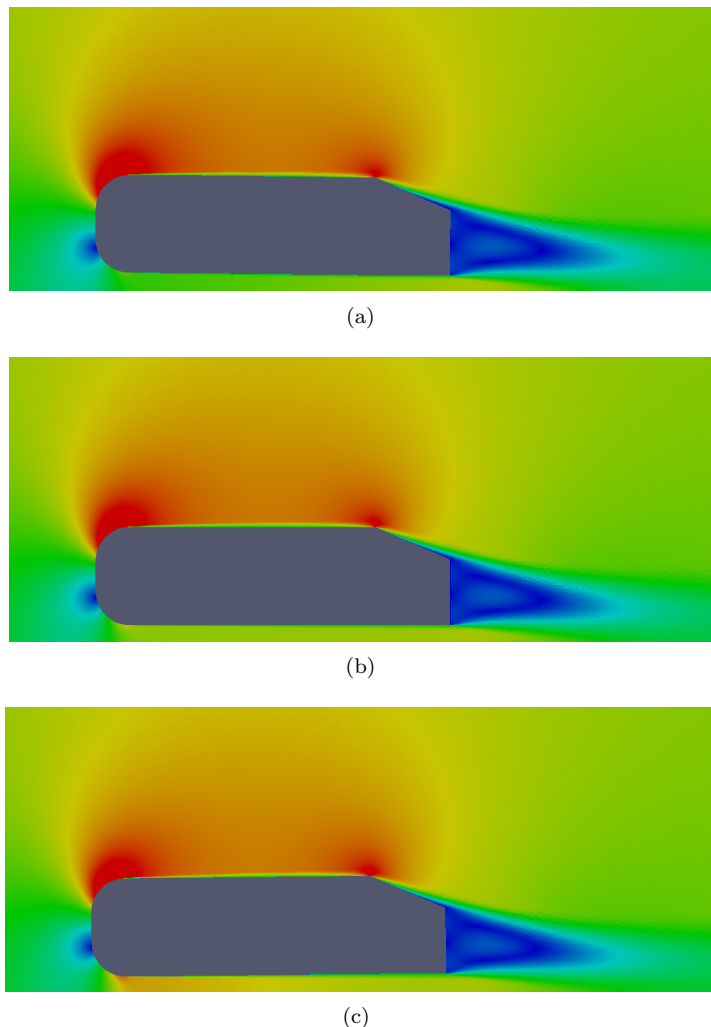


Figure 10. Steady state velocity fields from URANS simulations for three different geometries: Original (top), optimized and rebuilt (middle), and optimized and rebuilt, but without spoiler (bottom). The left column depicts the flow field when the jet is operational, the right column after it is switched off. For the two rebuilt geometries, note how the flow stays attached and is only slightly lifted up when the jet is switched off. The resulting drag coefficients are  $C_D = 0.4299$  for the original geometry (b), 0.1999 for the rebuilt with spoiler (d), and 0.2144 for the rebuilt without spoiler (f).

We can thus conclude that the optimized geometries stably support an attached flow regime: Once the flow is attached (e. g. by means of a suction jet), it stays attached. In order to further assess the stability of this regime, we now vary the angle of attack of the incoming flow: Two new cases are generated by rotating the body of the rebuilt geometry without spoiler by  $+0.5^\circ$  and  $-0.5^\circ$ , respectively. The rotation is propagated into the volume mesh by means of free-form deformation. For these two new cases, URANS

simulations are carried out, thereby using the attached flow of the non-rotated optimized geometry (Fig. 10f) as a seeding solution. As can be seen from Fig. 11, the flow stays attached also under these circumstances. Given that the difference in slant angle between the original and the optimized geometry is just  $1.8^\circ$  ( $23.2^\circ$  vs.  $25^\circ$ , see above), the confirmed stability corridor of at least  $\pm 0.5^\circ$  can already be regarded as significant. We will therefore not investigate if it can be extended any further.



**Figure 11. Stability of the attached flow w.r.t. changes in the angle of attack (AoA): Velocity fields for AoA =  $-0.5^\circ$  (a),  $0^\circ$  (b), and  $+0.5^\circ$  (c).**

The observation that it is just a slight variation of the slant angle that makes the difference between supporting two radically different flow regimes or only one, suggests to investigate the actual bandwidth of slant angles that support such a hysteresis behavior. To that end, URANS simulations were performed for various slant angles between  $0^\circ$  and  $30^\circ$ . When the flow exhibited a separation, a suction jet as before was applied until the flow reattached. Conversely, when the original flow did not separate, a blowing jet of similar strength was used to enforce separation. The jets were then switched off (typically after  $100\text{ ms}$ , as before) to see if the enforced flow solution was stable. It turned out that only a small bandwidth of angles support hysteresis (dashed lines in Fig. 12): The upper limit being the  $23.2^\circ$  as determined by the topology optimization and the lower limit being around  $22.6^\circ$ .

The geometry with the lowest drag (the star in Fig. 12) corresponds to the solution found by the topology optimization of section III. Starting from a detached flow at  $25^\circ$  degrees and  $C_D = 0.4299$ , the optimization went all the way to the other hysteresis branch. The obtained drag value of  $0.1999$  is smaller than any of the values of the attached hysteresis branch, because the topology optimization had the additional freedom of shaping the spoiler.

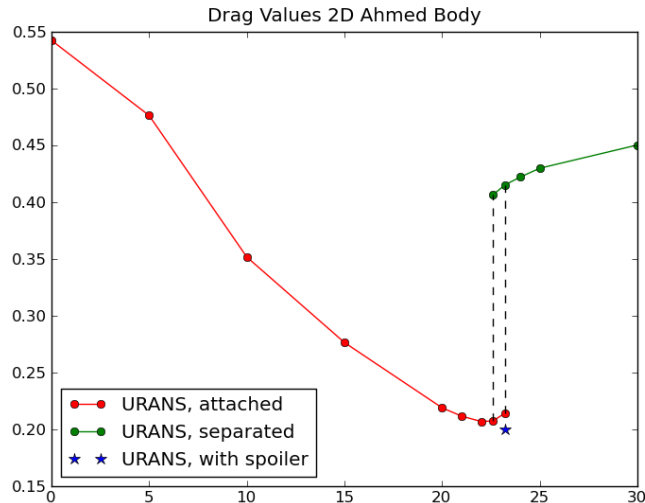


Figure 12. Ahmed body drag coefficient  $C_D$  vs. slant angle: Only a small bandwidth between  $22.6^\circ$  and  $23.2^\circ$  supports two solutions. The blue star corresponds to the geometry found by the topology optimization of section III.

## V. Conclusions

Judging from the results of our 2D study, topology optimization is a powerful tool also for external aerodynamics. We demonstrated its capability of discovering and exploiting hysteresis phenomena, which, in the present case, lead to a remarkable drag reduction with minimal geometric changes. While in ducted flow applications, the inherent design freedom of topology optimization tends to generate organic shapes that are sometimes difficult to manufacture, it is interesting to note that here, the optimization yielded simple and “straight” shapes when they are effective (the decreased slant angle), but also more elaborate shapes (the spoiler) if necessary for further improvement. In this respect it has the potential of being more effective than classical shape optimization.

The hysteresis phenomenon itself and the fact that it can be triggered by a technically feasible jet might be of practical interest in actual car aerodynamics. The sensible next step is therefore to extend the topology optimization study to 3D and to apply it to a production passenger car.

## Acknowledgments

The first author is grateful to Carlos R. Ilario da Silva and Thomas D. Economon for numerous enlightening discussions and to the members of the Aerospace Design Laboratory at Stanford University for their hospitality.

## References

- <sup>1</sup>Lions, J. L., *Optimal control of systems governed by partial differential equations*, Springer Verlag, New York, 1971.
- <sup>2</sup>Pironneau, O., “On optimum design in fluid mechanics,” *J Fluid Mechanics*, Vol. 64, 1974, pp. 97–110.
- <sup>3</sup>Jameson, A., “Aerodynamic design via control theory,” *J Scientific Computing*, Vol. 3, 1988, pp. 233–260.
- <sup>4</sup>Löhner, R., Soto, O., and Yang, C., “An adjoint-based design methodology for CFD optimization problems,” *AIAA-03-0299*, 2003.
- <sup>5</sup>Economon, T. D., Palacios, F., and Alonso, J. J., “A Coupled-Adjoint Method for Aerodynamic and Aeroacoustic Optimization,” *AIAA-2012-5598*, 2012.
- <sup>6</sup>Bendsoe, M. P. and Sigmund, O., *Topology Optimization: Theory, Methods and Applications*, Springer, 2004.
- <sup>7</sup>Borrvall, T. and Petersson, J., “Topology optimization of fluids in Stokes flow,” *Int J Num Meth Fluids*, Vol. 41, No. 1, 2003, pp. 77–107.
- <sup>8</sup>Moos, O., Klimetzek, F., and Rossmann, R., “Bionic Optimization of Air-Guiding Systems,” *SAE Technical Paper 2004-01-1377*, 2004.
- <sup>9</sup>“ToscaFluid<sup>®</sup>, <http://www.3ds.com/productsservices/simulia/products/tosca/fluid/>” 2017.

- <sup>10</sup>Gersborg-Hansen, A., Sigmund, O., and Haber, R., “Topology optimization of channel flow problems,” *Structural and Multidisciplinary Optimization*, Vol. 30, 2005, pp. 181–192.
- <sup>11</sup>Othmer, C. and Grahs, T., “Approaches to fluid dynamic optimization in the car development process,” *Proceedings of the EUROGEN Conference, Munich, Germany*, 2005.
- <sup>12</sup>Othmer, C., Kaminski, T., and Giering, R., “Computation of topological sensitivities in fluid dynamics: Cost function versatility,” *Proceedings of the ECCOMAS CFD Conference, Delft, The Netherlands*, 2006.
- <sup>13</sup>Othmer, C., “A continuous adjoint formulation for the computation of topological and surface sensitivities of ducted flows,” *Int J Num Meth Fluids*, Vol. 58, 2008, pp. 861–877.
- <sup>14</sup>Zymaris, A. S., Papadimitriou, D. I., Giannakoglou, K. C., and Othmer, C., “Continuous Adjoint Approach to the Spalart-Allmaras Turbulence Model for Incompressible Flows,” *Computers & Fluids*, Vol. 38, No. 8, 2009, pp. 1528–1538.
- <sup>15</sup>Zymaris, A. S., Papadimitriou, D. I., Giannakoglou, K. C., and Othmer, C., “Adjoint wall functions: A new concept for use in aerodynamic shape optimization,” *J Comput Physics*, Vol. 229, No. 13, 2010, pp. 5228–5245.
- <sup>16</sup>Kontoleonos, E. A., Papoutsis-Kiachagias, E. M., Zymaris, A. S., Papadimitriou, D. I., and Giannakoglou, K. C., “Adjoint-based constrained topology optimization for viscous flows, including heat transfer,” *Engineering Optimization*, Vol. 45, No. 8, 2013, pp. 941–961.
- <sup>17</sup>Othmer, C., “Adjoint methods for car aerodynamics,” *Journal of Mathematics in Industry*, Vol. 4, No. 1, 2014, pp. 1–23.
- <sup>18</sup>Helgason, E. and Krajnovic, S., “Aerodynamic shape optimization of a pipe using the adjoint method,” *Proceedings of the ASME 2012 International Mechanical Engineering Congress & Exposition, Houston, Texas, USA*, IMECE, 2012.
- <sup>19</sup>Lincke, A. and Rung, T., “Adjoint-based Sensitivity Analysis for Buoyancy-driven Incompressible Navier-Stokes Equations with Heat Transfer,” *Proceedings of the Eighth Internat. Conf. on Engineering Computational Technology, Dubrovnik, Croatia*, 2012.
- <sup>20</sup>Jakubek, D. and Wagner, C., “Shape Optimization of Train Head Cars using Adjoint-based Computational Fluid Dynamics,” *Proceedings of the First International Conference on Railway Technology, Las Palmas de Gran Canaria, Spain*, 2012.
- <sup>21</sup>Towara, M., “Numerical Optimization of an Oil Intake Duct with Adjoint Topological Methods,” *Diploma thesis, RWTH Aachen University, Dept. of Software and Tools for Computational Engineering*, 2011.
- <sup>22</sup>Hinterberger, C. and Olesen, M., “Automatic Geometry Optimization of Exhaust Systems Based on Sensitivities Computed by a Continuous Adjoint CFD Method in OpenFOAM,” *SAE Technical Paper 2010-01-1278*, 2010.
- <sup>23</sup>Hinterberger, C. and Olesen, M., “Industrial Application of Continuous Adjoint Flow Solvers for the Optimization of Automotive Exhaust Systems,” *Proceedings of the ECCOMAS Thematic Conf. – CFD & Optimization, Antalya, Turkey*, ECCOMAS, 2011.
- <sup>24</sup>Kondoh, T., Matsumori, T., and Kawamoto, A., “Drag minimization and lift maximization in laminar flows via topology optimization employing simple objective function expressions based on body force integration,” *Structural and Multidisciplinary Optimization*, Vol. 45, No. 5, 2012, pp. 693–701.
- <sup>25</sup>Ahmed, S. R., Ramm, R., and Falting, G., “Some salient features of the time-averaged ground vehicle wake,” *SAE Technical Paper 84-0300*, 1984.
- <sup>26</sup>“OpenFOAM<sup>®</sup>,” <http://www.openfoam.com>, 2017.
- <sup>27</sup>“HELYXAdjoint<sup>®</sup>,” <http://engys.com/technology/adjoint-cfd>, 2017.
- <sup>28</sup>de Villiers, E. and Othmer, C., “Multi-Objective Adjoint Optimization of Intake Port Geometry,” *SAE Technical Paper 2012-01-0905*, 2012.